Title

Numerical study of the chemo-mechanical behavior of FEBEX bentonite in nuclear waste disposal based on the Barcelona expansive model

Authors

Xu, Hao

Zheng, Liange

Rutqvist, Jonny

et al.

Publication Date

2021-04-01

DOI

10.1016/j.compgeo.2020.103968

Peer reviewed

Numerical study of the Chemo-Mechanical Behavior of FEBEX Bentonite in Nuclear Waste Disposal Based on the Barcelona Expansive Model

Hao Xu[a,*], Liange Zheng[a], Jonny Rutqvist[a], Jens Birkholzer[a]

[a]*Energy Geosciences Division, Earth & Environmental Sciences Area, Lawrence Berkeley National Laboratory, Berkeley, CA 94720*

Abstract

Experimental studies show that compacted bentonite used as a backfill material for nuclear waste repository experiences strong coupling between chemical and mechanical processes. Therefore, a rigorous description of such coupling and evaluation of its implication to the long term behavior of bentonite buffer in the repository are required. In this paper, we use a dual-structure expansive soil model, referred to as the Barcelona Expansive Model (BExM), to predict the behavior of bentonite buffer in subsurface emplacement tunnels for high-level radioactive waste. After emplacement, the bentonite is subjected to complex and coupled Thermal-Hydraulic-Mechanical-Chemical (THMC) processes. The BExM constitutive model is implemented in a multi-phase reactive transport and geomechanics simulator, TOUGHREACT-FLAC3D, and the model is verified with one benchmark test on FEBEX bentonite. We utilize a one-way Chemo-Mechanical (C-M) coupling approach, in which chemical changes affect the mechanical

*Corresponding author
Email address: haoxu@lbl.gov (Hao Xu)

behavior of bentonite through the BExM linked with the evolution of mass fraction of smectite, exchangeable cation concentration, and ionic strength via osmotic suction. The parameters of the new coupled model for FEBEX bentonite are calibrated against a series of laboratory experiments with various salinity solutions. Finally, a numerical analysis of a generic case of heating experiment with FEBEX bentonite under coupled THMC processes is conducted and the simulated results are physically interpreted.
Keywords:
Compacted bentonite, nuclear waste, BExM, chemo-mechanical coupling

1. Introduction

Bentonite (or a mixture of bentonite and other materials) is often considered as a buffer material in the Engineered Barrier System (EBS) of geological repositories for high level radioactive waste. Bentonite has an important safety function providing a physical protection of the waste packages emplaced in underground tunnels, due to its high swelling capacity, low permeability, and strong capability of retarding the migration of radionuclides. After emplacement tunnels are loaded with waste packages and backfilled with bentonite, the buffer material undergoes heating from the waste packages and hydration from host rocks, and is affected simultaneously by Thermal-Hydraulic-Mechanical-Chemical (THMC) processes. It is important that these coupled processes are well understood and their impacts on long-term performance of the EBS can be well predicted. Numerical modeling is an indispensable tool in this context, as the safety of the repository has to be ensured for 100,000 years or longer. However, simulating the coupled

THMC processes in bentonite is challenging, in part because the constitutive relationship of individual process is complex and hard to obtain while at the same time the choice of constitutive relationships and their parameterization has a strong impact on the simulation results.

Model interpretation of field tests and laboratory experiments, integrated with microscopic observation, is an effective way to conceptualize and verify constitutive relationships for bentonite. Many field experiments have been conducted to investigate the evolution of bentonite buffer in a condition similar to a geological repository, and large monitoring data have been collected that can be used for model testing and uncertainty quantification. For example, the *in situ* heating test within the Full-scale Engineered Barriers EXperiment (FEBEX) project [1] was running in the Grimsel Test Site for 18 years, between 1997 and 2016. The Grimsel Test Site is an underground research laboratory situated in the Swiss Alps, featuring multiple research tunnels established in a granite host rock. Other examples include the HE-E *in situ* heating test [2] and the large scale "Engineered Barrier" (EB) experiment, both performed in the Mont Terri Underground Laboratory [3] and situated in argillaceous clay host rock. Meanwhile, a number of small scale experiments have been carried out in the laboratory to investigate the soil properties in detail. These include, Tripathy *et al.* [4] and Villar [5] who addressed the behavior of compacted expansive soils under swell-shrink cycles as well as Komine and Ogata [6] who performed laboratory experiments to study fundamental characteristics of compacted bentonite. Observations from such experiments show that the swelling deformation is strongly dependent on the initial dry density, confining pressure, and initial water con-

tent. Ultimately the swelling characteristics of bentonite is determined by its micro-structural clay minerals ((i.e. montmorillonite) [4]. To quantitatively describe this swelling behavior, additional equations were derived to account for micro-scale characteristics such as the distance between two montmorillonite layers, the ion concentration of the pore water, the specific surface of bentonite, and repulsive and attractive forces [7]. Stawinski *et al.* [8] examined the micro-structure of bentonite with various concentrations of different cations using scanning electron microscope techniques, and found that the radii and micro-structure of the aggregates (stacks of clay minerals) were influenced by the concentrations of cations. Saiyouri *et al.* [9] studied the swelling of highly compacted clay in response to hydration, and found that the clay begins to swell as a result of adsorption of water between layers of clay minerals and a subdivision of the clay particles. Mercury Intrusion Porosimetry (MIP) tests have been performed on sodium bentonite clay, and a bimodal pore size distribution, referred to as the dual-structure, is found inside the compacted bentonite samples [10]. A similar behavior was observed and reported for MX-80 bentonite [11].

During the last two decades, most simulation approaches for interpreting laboratory and field experiments on bentonite relied on coupled Thermal-Hydraulic-Mechanical (THM) models using a variety of constitutive relationships for the mechanical behavior of bentonite. To account for the unsaturated conditions of soils, researchers have used soil mechanics models for saturated soil, such as the Modified Cam-Clay model, and expanded those to unsaturated by considering the effect of saturation or suction on soil strength and stiffness [12, 13]. Examples include the Barcelona Basic

Model (BBM) [14], and the Barcelona Expansive Model (BExM) [15], as well as other Cam-Clay like constitutive models [16, 17, 18, 19]. Gens *et al.* [20] used the BBM to study THM processes of bentonite in the FEBEX *in situ* test, with special attention on the hydration of bentonite as affected by heating and vapor transport, and on the development of swelling pressure in the bentonite barrier. Rutqvist *et al.* [21] implemented the BBM into the TOUGH-FLAC3D simulator and applied it to study thermal and hydraulic behavior of FEBEX bentonite in a generic argillite repository [22]. The BBM has also been widely used or extended by other researchers [23, 24, 25] for predicting more sophisticated THM behavior of unsaturated soils. ACMEG-TS, a constitutive model developed by François and Laloui [19] for unsaturated soils under non-isothermal conditions, was later used by Dupray *et al.* [26] to study the relevant temperature and suction effects on elasto-plasticity of FEBEX bentonite. The BExM [15, 27, 28] is an extension of BBM that considers the interaction between a capillary controlled macro-structure and a micro-structure where the swelling behavior is described at the particle level. The BExM was used in THM models to simulate a mock-up test conducted as part of the FEBEX project [29] and has also been applied for generic nuclear waste disposal studies of buffer resaturation [30]. An international cooperative project entitled DECOVALEX (an acronym for DEvelopment of COupled models and their VALidation against EXperiments) was established in 1992 by a number of national regulatory authorities, to cooperate in developing and testing models capable of simulating coupled processes. In this collaboration project, THM models for bentonite-rock systems [31] was one of the major themes and a variety of constitutive models for mechanical

behavior were developed, including models using the BBM and the BExM approaches.

So far, only few modeling studies focusing on THM processes in bentonite have included chemical effects, in part because fully coupled THMC processes are difficult to study experimentally and difficult to incorporate in numerical models. The early theoretical research of coupled THMC processes by Ulm and Coussy [32] and Coussy and Ulm [33] introduce the chemical potential into the thermodynamic framework of a reactive porous continuum to investigate the creep and plastic behavior of early-age concrete due to thermo-chemo-mechanical couplings. Chemical dissipation is taken into account by the affinity of the chemical reaction, and the conjugated reaction rate. Later, this framework was extended to full THMC couplings for general porous media [34]. A similar method has been used to study oil/gas production by incorporating the solute concentration into a mechanical equilibrium equation [35] and to study CO_2 sequestration processes with indirect chemo-mechanical (C-M) couplings [36]. Sherwood [37] modified the thermodynamics variables in the Biot theory of poro-elasticity to include the chemical potential of all chemical species within the pore fluid. The purpose of that work was to study osmotic effects in shale to investigate possible swelling induced disintegration in the process of drilling. Sequential coupling methods have been developed for geothermal systems [38, 39] and nuclear waste disposal [40], thereby utilizing a linear C-M coupling model to analyze the swelling of bentonite [22, 40]. Guimarães *et al.* [41] developed a C-M constitutive model by incorporating osmotic suction and exchangeable cations into a dual-structure model. By extending the C-M coupling model proposed by

[42] for saturated homoionic expansive clay, Lei *et al.* [43, 44] formulated a THMC coupling model for unsaturated expansive clay by proposing generalized effective stress as a driving force with suction and chemical effects based on a rigorous thermodynamic framework.

In this work, we present another approach to investigate C-M coupling within the THMC model. Unlike previous works (e.g. Zheng *et al.* [40, 45]), we use the BExM to link three types of chemical effects to mechanical processes. In terms of C-M coupling approach, we follow the approach of Guimarães *et al.* [41], and add a term of smectite mass fraction into BExM to directly account for the effect of the abundance of swelling clay on welling pressure in addition to two chemical effects - the concentration of exchangeable cations and ionic strength that are already in the approach of Guimarães *et al.* [41]. Adding the effect of abundance of swelling clay minerals (smectite or montmorillonite) on swelling may seem marginal, but it is critical for evaluating the long term C-M behavior in bentonite buffer for high level waste repository. After verifying the constitutive relationship and calibrating model parameters for FEBEX bentonite, we develop coupled THMC models under high temperature for a generic case of argillite repository with bentonite buffer, in contrast to that the approach previously was used mostly to coupled Mechanical-Chemical (MC), or Hydraulic-Mechanical-Chemical (HMC) with one single phase fluid, or THM processes. The THMC modeling illustrates the effect of chemical change on the mechanical processes when a more complicated C-M coupling strategy is used than previous works [40, 45]. Our paper is organized as follows: firstly, Section 2.1 and Section 2.2 summarize all governing equations and an short introduction of the

mechanical constitutive model whose detailed variables and equations are summarized in Appendix A. Section 2.3 presents one benchmark example to verify the model implementation. Section 3 explains the C-M coupling strategy and describes the calibration of model parameters against laboratory experiments. Finally, a coupled THMC model for a generic argillite repository with bentonite is presented in Section 4.

2. Modeling Approach, Governing Equations, and Constitutive Relationships

2.1. Governing equations

The expansive soil is represented as a continuum porous media consisting of three mass components: water, air, and clay. Within the material, three phases are considered in the domain: solid (s), liquid (l) and gas (g). The solid phase is composed of the skeleton of clay, the liquid phase includes liquid water and dissolved dry air, and the gas phase contains dry air and water vapor. The mass and energy balance equations can be expressed in a general form as

$$\frac{\mathrm{d}}{\mathrm{d}t}M^{\gamma} = -\boldsymbol{\nabla}\cdot\mathbf{F}^{\gamma} + q^{\gamma}, \tag{1}$$

where the symbol γ can represent three mass components and heat term (h); $\boldsymbol{\nabla}\cdot$ is the divergence operator; M^{γ} denotes the storage or accumulation term, in terms of mass or energy per volume; $\mathbf{F}^{\gamma}$ denotes the mass or heat flux; and q^{γ} denotes the sinks and sources. In the absence of other external sinks or sources in the porous media system, the summation of all sink/source terms vanishes.

For the solid part, the storage and flux term in Equation (1) are calculated as

$$M^s = \rho_s(1-\phi), \tag{2}$$

$$\mathbf{F}^s = (1-\phi)\rho_s \mathbf{v}_s. \tag{3}$$

Here ϕ is the porosity, ρ_s is the density of solid skeleton, and $\mathbf{v}_s$ is the velocity of the solid skeleton.

The momentum balance equation for the solid skeleton is obtained from equilibrium:

$$\boldsymbol{\nabla} \cdot \boldsymbol{\sigma}^{total} + \rho_m \mathbf{g} = \rho_m \frac{\mathrm{d}\mathbf{v}_s}{\mathrm{d}t}, \tag{4}$$

where $\boldsymbol{\sigma}^{total}$ is the Cauchy stress tensor. To be consistent with the total stress in poro-mechanics, we note it with the superscript "*total*" here. ρ_m is the average density of the porous media, $\mathbf{g}$ is the gravitational acceleration, and t is the time.

For fluid flow, the accumulation term is expressed as

$$M^f = \phi \sum_{\xi} S_\xi \rho_\xi X_\xi^f. \tag{5}$$

The total mass of the flow component f is the summation over two fluid phases: liquid (l) and gas (g). For phase ξ, S_ξ is the associated saturation, ρ_ξ is the density, and X_ξ^f is the mass fraction of component f present in that phase.

The fluid flux contains advection ($\mathbf{F}_{adv}^\kappa$) and non-advection ($\mathbf{F}_{dis}^\kappa$, e.g. diffusion or dispersion). Advective flux is the summation over phases and the corresponding phase flux can be calculated by Darcy's law as follows

$$\mathbf{F}_{adv}^{f} = \sum_{\xi} X_{\xi}^{f} \mathbf{F}_{\xi}, \tag{6}$$

$$\mathbf{F}_{\xi} = -\mathbf{k}\frac{k_{r\xi}\rho_{\xi}}{\mu_{\xi}}\left(\nabla p_{\xi} - \rho_{\xi}\mathbf{g}\right), \tag{7}$$

where $\mathbf{k}$ is the absolute permeability; $k_{r\xi}$ is the relative permeability to phase ξ; μ_{ξ} is the viscosity; and p_{ξ} is the fluid pressure in phase ξ. ∇ is the gradient operator.

The dispersion is given as

$$\mathbf{F}_{dis}^{f} = -\sum_{\xi} \rho_{\xi} D_{v} \nabla X_{\xi}^{f}, \tag{8}$$

where D_v is an effective diffusion coefficient that depends on temperature, gas pressure, medium tortuosity, and gas saturation.

Similarly, the heat storage term in a multiphase system is

$$M^{h} = (1-\phi)\rho_{s} C_{s} T + \phi \sum_{\xi} S_{\xi}\rho_{\xi} u_{\xi}, \tag{9}$$

where C_s is the specific heat of the solid skeleton; T is the temperature; and u_{ξ} is the specific internal energy in phase ξ. The heat flux studied here is assumed to include conduction and convection terms:

$$\mathbf{F}^{h} = -\lambda_{t}\nabla T + \sum_{\xi} h_{\xi}\mathbf{F}_{\xi}, \tag{10}$$

where λ_t is the thermal conductivity; and h_{ξ} is the specific enthalpy in phase ξ.

2.2. Mechanical constitutive model

The mechanical constitutive model used in this study accounts for the dual-structure of compacted bentonite. As Figure 1(a) shows, based on MIP tests by Lloret *et al.* [46], two pore size families can be clearly observed in compacted bentonite, with a micro-structure defined by pore sizes below 130 nm and a macro-structure above this threshold. The micro-structure is formed by clay minerals and micro-pores, and the macro-structure consists of clay particles and macro-pores between them (Figure 1(b)). To capture this feature of unsaturated soils, Gens *et al.* [15] developed a dual-structural model, referred to as BExM, by incorporating a micro-structure representation into the original elasto-plasticity model, BBM. As the material is divided into micro- and macro-structures, swelling occurs at the micro-structure, which will invade into the macro-structure and induce additional plastic deformations. Equations to describe the mechanical behavior of micro-structural and macro-structural levels and the interaction between two structural levels and corresponding variables are summarized in Appendix A.

2.3. Verification of the mechanical model

The dual-structure model is implemented into the geomechanics simulator FLAC3D by using the User Defined constitutive Model (UDM) option with C++ dynamic link libraries. In this section, we present one case with a combination of loading paths on compacted bentonite samples to verify the model implementation. The numerical analyses are launched with a set of material parameters calibrated against laboratory experiments from published literature.

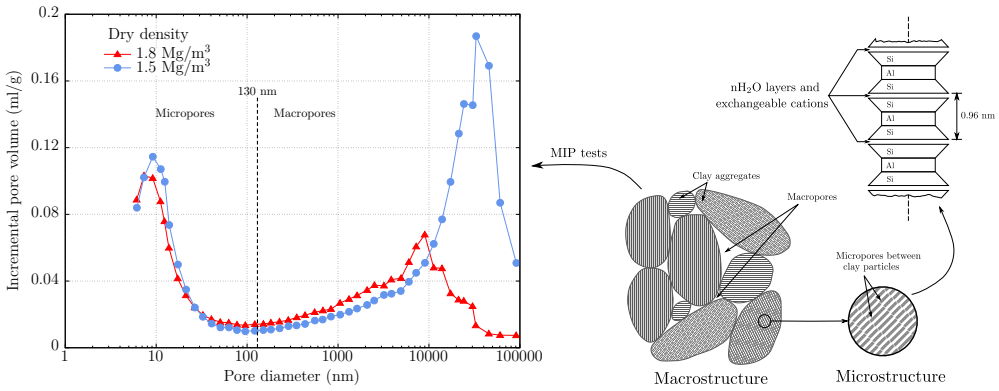

(a) (b)

Figure 1: (a) Pore size distribution of the compacted material (Data from [46]), and (b) Schematic representation of the two structural levels (Adapted from [30] and [47]).

2.3.1. Tests with a combination of loading paths

Two oedometer tests on FEBEX bentonite carried out at the Centro de Investigaciones Energéticas, Medioambientales y Tecnológicas (CIEMAT) Laboratory with suction control are simulated with BExM. A combination of loading paths including confinement stress change and suction change presented in Table 1 were applied in these two tests. The samples were initially compacted to a dry density of 1.70±0.02 g/cm^3 with the material at about 13.0% water content. The parameters of BExM used in our simulation are the same as those calibrated by [46] and shown in Table 2.

Tests S1 and S5 share the same initial and similar final stress states but with different loading paths. As Figure 2 displays, firstly, test S1 and test S5 were both dried under the same vertical stress to the reference suction at point B. Then test S1 was loaded to a 5.1 MPa vertical stress under a constant suction of 550 MPa, and later wetted to full saturation, while test

Table 1: Stress paths of the tests performed at CIEMAT Laboratory [46].

Test	Path							
	A		B		C(S1) or D(S5)		E	
	σ_v MPa	s MPa	σ_v MPa	s MPa	σ_v MPa	s MPa	σ_v MPa	s MPa
S1	0.1	138	0.1	550	5.1	460	5.1	0
S5	0.1	138	0.1	520	0.1	0	5.0	0

Table 2: Parameters used for the verification case [46].

Parameters defining the Barcelona Basic Model for macro-structural behavior							
$\kappa = 0.005$	$\kappa_s = 0.001$	$\lambda(0) = 0.08$	$p_c = 0.5$ MPa	$r = 0.90$	$\zeta = 1$ MPa^{-1}	$p_0^* = 12$ MPa	
Parameters defining the law for micro-structural behavior							
$\alpha_m = 0.021$ MPa^{-1}	$\beta_m = 2.3 \times 10^{-3}$ MPa^{-1}	$\chi = 1$					
Interaction functions							
$f_{ic} = 1 + 0.9 \tanh\left[20\left(\frac{p_r}{p_0} - 0.25\right)\right]$				$f_{is} = 0.8 - 1.1 \tanh\left[20\left(\frac{p_r}{p_0} - 0.25\right)\right]$			
Initial conditions							
$e_{\text{macro}} = 0.11$				$e_{\text{micro}} = 0.45$			

S5 was wetted to saturation under constant vertical stress and then loaded to a vertical stress of 5.0 MPa. Figure 3 shows the numerical results and experimental observations of void ratio evolution over the stress paths and over suction changes for the two tests. As Lloret *et al.* [46] suggested, in order to use a logarithmic scale, a constant value of 0.1 MPa has been added to all suction values plotted in figures with suction changes.

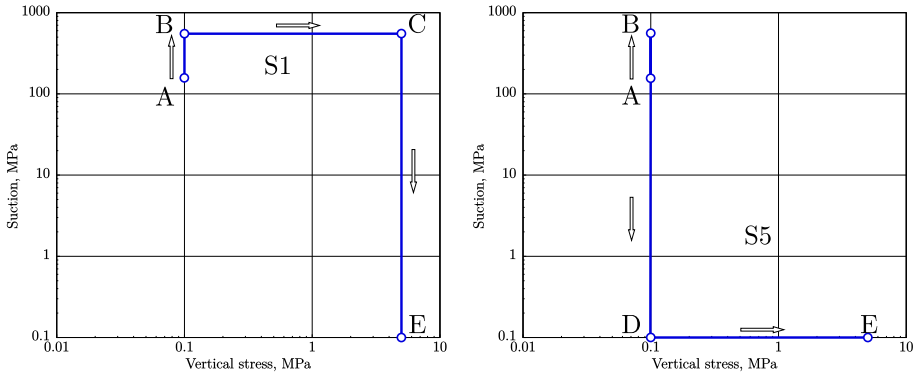

(a) Test S1. (b) Test S5.

Figure 2: Stress paths of tests (a) S1 and (b) S5 [46].

The blue lines in Figures 3(a) and 3(b) represent the computed total void ratio against stress changes and suction changes for test S1. Both figures show that the numerical results match the experimental data very well. Figure 4(a) displays the computed micro-structural and macro-structural void ratios over suction loading, respectively. Figure 5(a) illustrates the evolution of the interaction function in test S1. In the path from B to C, the interaction

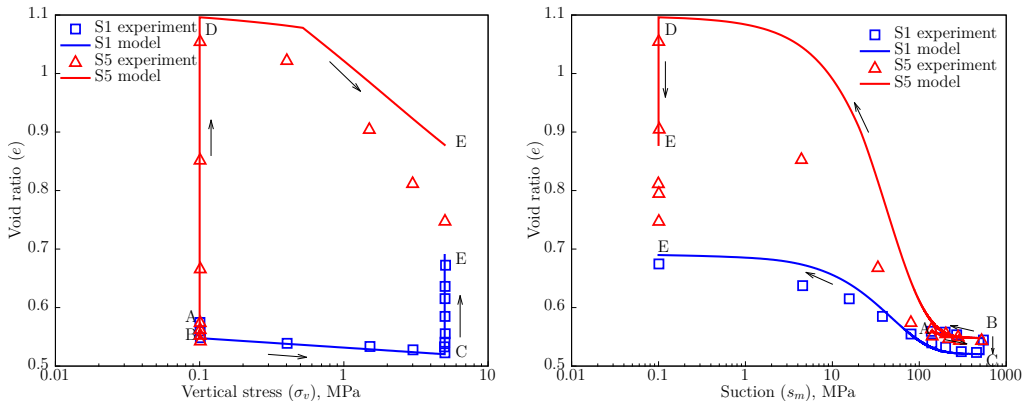

(a) Variation of void ratio over stress paths. (b) Variation of void ratio over suction changes.

Figure 3: Experimental results [46] and computed variation of void ratio for tests S1 and S5.

function shows the sample follows the Micro-structural Compression (MC) path, and both micro- and macro-structural strains are very small due to the high stiffness under high suction. During the wetting stage from C to E, the micro-structure swells due to hydration while the macro-structural strain is small. The interaction function is negative before reaching point E, indicating the macro-strain induced by micro-strain is contraction. As a result of that, the total void ratio change is mainly caused by the contribution of micro-structural swelling.

The behavior of test S5 is different from test S1. Computed total void ratio for test S5 against vertical stress changes and against suction changes are plotted in Figure 3(a) and Figure 3(b) with red lines. The evolution of the micro-structural and macro-structural void ratio computed for test S5 is displayed in Figure 4(b). Figure 5(b) shows the evolution of the interaction functions in test S5. Similar to test S1, the first drying process in test S5 from

A to B does not induce much void ratio change. Then, during the following swelling stage from B to D, the micro-structure swells, inducing larger plastic strains in the macro-structure (Figure 4(b)) because of a large positive value of the interaction function f_{is} (Figure 5(b)). In the final loading stage from D to E, since the specimen is saturated, the compressive strains induced by the external loading stems mainly from the macro-structural deformation.

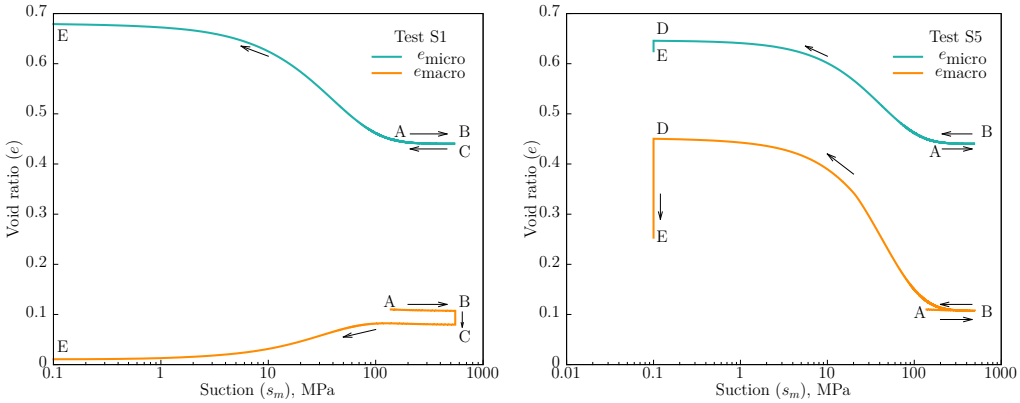

(a) Test S1 (b) Test S5

Figure 4: Evolution of computed macro-structural and micro-structural void ratio for tests S1 and S5.

Compared to test S1, in which the stress loading process (path B to C in Figure 3(b)) before the hydration process suppresses the swelling deformation, the drying process in test S5 (path A to B in Figure 3(b)) without stress loading enhances the swelling deformation. In general, a good reproduction of the experimental behavior by the model results is achieved for test S1 and S5, except some deviations are observed at intermediate and final stages of

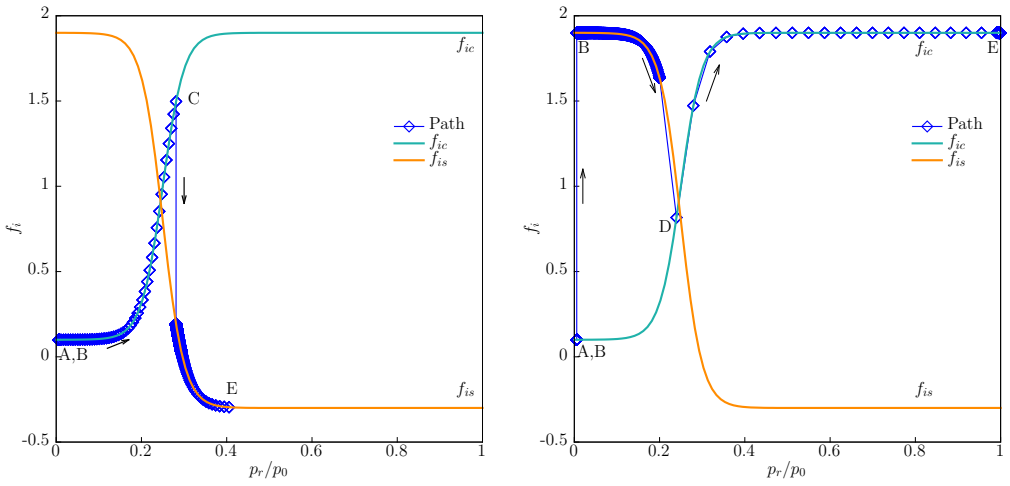

(a) Test S1 (b) Test S5

Figure 5: Interaction involved in the various stages of tests S1 and S5.

the swelling of test S5.

3. Chemo-Mechanical Coupling

The coupling between chemical and mechanical processes allows us to evaluate the direct impact of chemical changes on mechanical behavior. In our previous THMC modeling work [48], the C-M coupling was carried out via an extended linear swelling model, in which the swelling pressure is linearly related to liquid saturation [49, 22], total ion concentration of pore water, and mass fraction of swelling clay [50, 51]. The advantage of such method is that the coefficients are relatively easy to calibrate. The disadvantage is, however, that such a phenomenological model does not accurately describe the micro-scale physics of swelling. It neglects the transient history of mechanical change and is unable to account for the impact of cation exchange reactions

on the swelling process. Here, we use BExM [28] to link the chemical and mechanical processes.

3.1. Chemo-Mechanical coupling scheme

In Guimarães *et al.* [41], the swelling of unsaturated bentonite was investigated for two chemical effects, osmotic suction and exchangeable cations. However, the swelling of bentonite is also dictated by the abundance of smectite–the reason why Kunigel-VI bentonite has a lower swelling pressure than FEBEX bentonite [40]. Zheng *et al.* [48] have collected experimental data on different types of compacted bentonite and obtain a linear regression of swelling pressure versus smectite mass fractions for each bentonite. In the current THMC model, we therefore factor the abundance (represented by mass fraction) of smectite into the BExM. Thus, in our model, chemical changes affect mechanical behavior of bentonite through the evolution of abundance of smectite, exchangeable cation concentration, and ionic strength via osmotic suction. The mathematical formulations for such C-M coupling are summarized below.

The mass fraction of smectite, f_s, is introduced into the micro-structure part of BExM. The swelling capacity of the material should decrease with the reduction in the mass fraction of smectite. The dependence of micro-structural volumetric strains on the change in the micro-structural effective stress is therefore formulated as follows:

$$\mathrm{d}\varepsilon^{e}_{vm} = \frac{f_s}{K_m}\mathrm{d}\hat{p}. \tag{11}$$

This equation replaces Equation (A.19) to consider the effect of smectite directly. The effect of ionic strength of the pore water on micro-structural

strain is carried out via the osmotic suction, which is included in the effective stress. The osmotic suction is computed as [41]

$$s_o = -10^{-6}\frac{RT}{V_w}\ln a_w, \tag{12}$$

where V_w is the molar volume of water in m^3/mol; and a_w is the activity of water, which is calculated in TOUGHREACT [52] as follows:

$$\ln a_w = -\Phi m^* \frac{1}{55.51}. \tag{13}$$

Here Φ is the osmotic coefficient of the solution and m^* is the sum of the molalities of all species in solution.

K_m in Equation (11), is calculated by Equation (A.21). The effect of exchangeable cations is linked to mechanics through the dependence of β_m on exchangeable cation concentration calculated with the following equation [53, 41]:

$$\beta_m = \sum_i \beta_m^i x_i, \tag{14}$$

where x_i is the equivalent fraction of the exchangeable cation i. Gens [53] and Guimarães *et al.* [41] proposed that β_m^i is proportional to the ionic hydrated radius and inversely proportional to its valence. β_m is the sum over ionic species.

The newly introduced mass fraction of smectite, f_s, is in the solid bentonite samples. As Figure 1(b) displays, the mineral structure of smectite will allow water to come into the sheet layers, which is the pre-condition for swelling. While the concentration of exchangeable cations, the term β_m^i, is

about the cations in the solution, specifically, it only accounts for the cations in the interlayer space of bentonite. Thus, the mass fraction of smectite and the concentration of exchangeable cations are different physical effects related to the selling behavior of compacted bentonite. Moreover, the mass fraction of smectite in compacted bentonite is easy to measure at the laboratory. However, with this modification, we need to recalibrate the values of β_m^i for different cations against laboratory experiments.

3.2. Simulator

The numerical simulations in this study are conducted with TOUGHREACT-FLAC3D, which sequentially couples the multiphase fluid flow and reactive transport simulator, TOUGHREACT [52], with the finite difference geomechanical code FLAC3D [54]. The coupling of TOUGHREACT and FLAC3D was initially developed in [49] to provide the necessary numerical framework for modeling coupled THMC processes with a linear elastic swelling model. Figure 6 shows the sequential coupling scheme of TOUGHREACT-FLAC3D. In each time step, TOUGHREACT calculates the primary variables for THC processes including temperature (T), liquid pressure (p_l) or gas pressure (p_g), matric suction (s_m) and concentration of exchangeable cations and/or abundance of swelling clay minerals (x_i). These primary variables are then passed to FLAC3D via a coupling module to conduct stress and strain analysis. The coupling between THC processes provided by TOUGHREACT and the mechanical part is carried out in FLAC3D at every time step. The mechanical computation is quasi-static, so the length of time step is constrained by the chemical calculation to accommodate small changes in the concentrations.

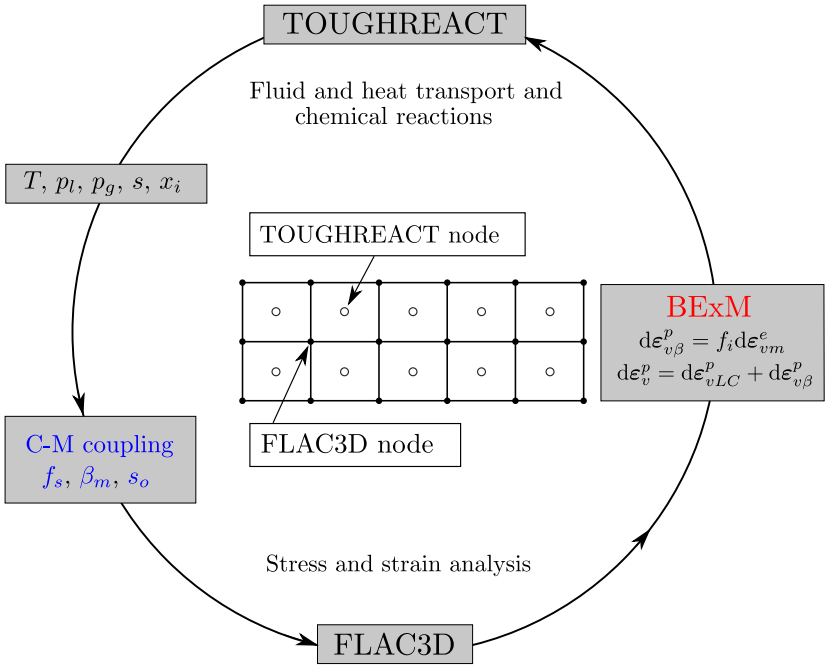

Figure 6: The coupling scheme for TOUGHREACT-FLAC3D (Adopted from reference [40]).

3.3. Calibration of the model against laboratory experiments

A set of parameters have to be calibrated such that the new C-M coupling in BExM can accurately describe the state of FEBEX bentonite. We performed a series of simulations on swelling pressure tests by Castellanos *et al.* [55] to do this calibration. These swelling pressure tests were operated under constant volume conditions. All samples were prepared at an initial suction of 98 MPa and a low vertical stress. Then a wetting path was followed, in which samples were saturated by four different salinity solutions while the suction was reduced to 0 MPa. During the experiment, the swelling pressure caused by the saturation was recorded with time. The numerical model represents the Hydraulic-Mechanical-Chemical (HMC) process during which the swelling pressure was measured. The hydrological and chemical parameters for FEBEX bentonite are given in Table 4, 5, and 8 in Section 4.1.

The four salinity solutions utilized to saturate the bentonite samples were distilled water, 0.1 mol NaCl, 2.5 mol NaCl, and 5.5 mol NaCl [55]. As water infiltrates into the samples, chemical disequilibrium causes minerals dissolution/precipitation, cation exchange, and aqueous complexation to occur. The initial mineral and pore water compositions are listed in Table 4 and 5 further below, and details of how those reactions are formulated and calculated are given in the manual of TOUGHREACT [52]. Evolution of mass fraction of smectite and the osmotic suction is obtained from the chemical model and does not need to be calibrated. In contrast, parameters that need to be calibrated are the β_m^i values of each minerals and macro-structural elastic stiffness parameters, κ and κ_s. The calibrated values for these param-

eters are listed in Table 3. The void ratios e_{micro} and e_{macro} are given by the experiment data reported in Sánchez *et al.* [28].

Table 3: Parameters of BExM for FEBEX bentonite (most are from [28]).

Parameters defining the Barcelona Basic Model for macro-structural behavior					
$\kappa = 0.03$	$\kappa_s = 0.006$	$\lambda(0) = 0.08$	$p_c = 0.5$ MPa	$r = 0.90$	$\zeta = 1$ MPa^{-1}	$p_0^* = 6.5$ MPa
$\alpha_a = 0.5$	$\alpha_0 = 1 \times 10^{-5}{}^{\circ}$C	$\beta_m^{Na} = 2.574 \times 10^{-9}$ MPa^{-1}	$\beta_m^{K} = 0.257 \times 10^{-9}$ MPa^{-1}			
$\beta_m^{Mg} = 3.346 \times 10^{-9}$ MPa^{-1}		$\beta_m^{Ca} = 2.574 \times 10^{-9}$ MPa^{-1}				
Parameters defining the law for micro-structural behavior						
$\alpha_m = 0.021$ MPa^{-1}	$\chi = 1$					
Interaction functions						
$f_{ic} = 1 + 0.9 \tanh\left[20\left(\frac{p_r}{p_0} - 0.25\right)\right]$		$f_{is} = 0.8 - 1.1 \tanh\left[20\left(\frac{p_r}{p_0} - 0.25\right)\right]$				
Initial conditions						
$e_{macro} = 0.24$	$e_{micro} = 0.45$	$f_s = 0.5428$	$s_0 = 0.777$ MPa			

Our simulation results in general are in good agreements with the observed decreases in the swelling pressure due to salinity changes (Figure 7), but the agreement is not as good for the case with 2.5 mol NaCl, where the simulated swelling pressure is about 0.7 MPa higher than the experimental measurement; moreover, the stress evolution deviates from what the data show at the beginning due to the non-zero compressive stress required by BExM, and the time evolution of swelling pressure is slower than the experimental observations.

Note that Castellanos *et al.* [55] also measured vertical swelling strains of bentonite under constant vertical stress when samples were saturated with $CaCl_2$ solutions. They obtained almost equal swelling strains for $CaCl_2$ and NaCl solutions with identical salinity, which indicates that it may be reason-

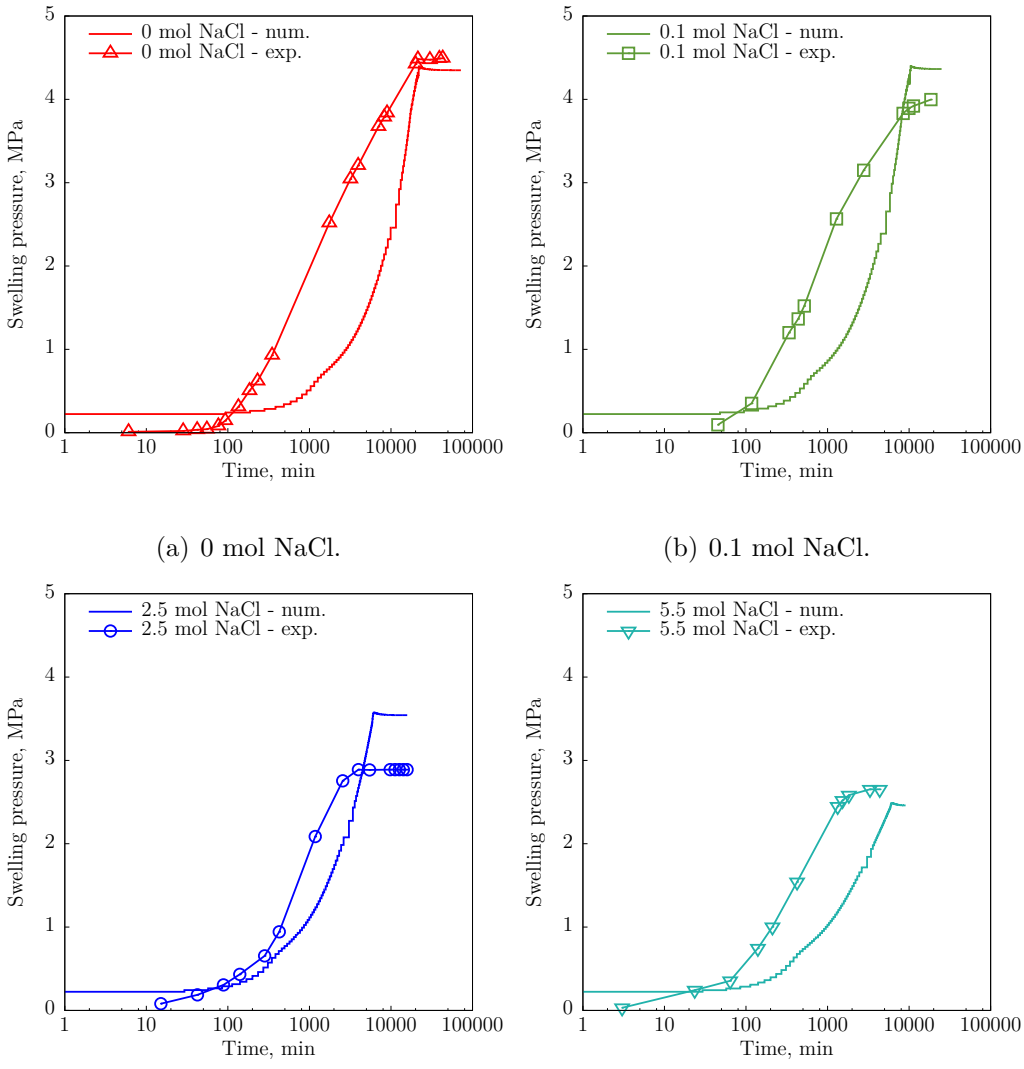

(a) 0 mol NaCl.

(b) 0.1 mol NaCl.

(c) 2.5 mol NaCl.

(d) 5.5 mol NaCl.

Figure 7: Simulation results of swelling pressure with different salinity solutions.

able to assume $\beta_m^{Na} = \beta_m^{Ca}$ as listed in Table 3.

4. Application to A Generic Repository

This section presents the coupled THMC model for a generic repository, focusing on mechanical changes induced by the chemical alteration in FEBEX bentonite used as a buffer/backfill material for waste canisters emplaced in an argillite host rock.

4.1. Model description

The model is applied to a hypothetical bentonite-backfilled nuclear waste repository in an argillaceous clay host rock, a repository example that involves a series of parallel horizontal nuclear waste emplacement tunnels at 500 m depth (Figure 8) [22]. The model is a pseudo-2D model (a 3D model with one layer of elements) with the z-axis pointing upward, the horizontal x-axis perpendicular to the emplacement tunnel, and the y-axis aligned with the tunnel axis. Based on symmetry considerations, the model domain considers only one emplacement tunnel and the half-space between tunnels. Note that while the canister is modeled as a heat source with mechanical properties of steel, the Thermal-Hydraulic-Chemical (THC) changes in the canister material and their interactions with EBS bentonite are not considered here for the sake of simplicity.

The initial hydrostatic stress come from an existing site at Mont Terri [22]. The average density of the rock formation is 2,700 kg/m^3. The vertical stress is from the self-weight of the rock, the ratios of the major horizontal stress (σ_{xx}) and the minor horizontal stress (σ_{yy}) to the vertical stress are 2.4 and 0.8 , respectively. Zero normal displacements are prescribed on the

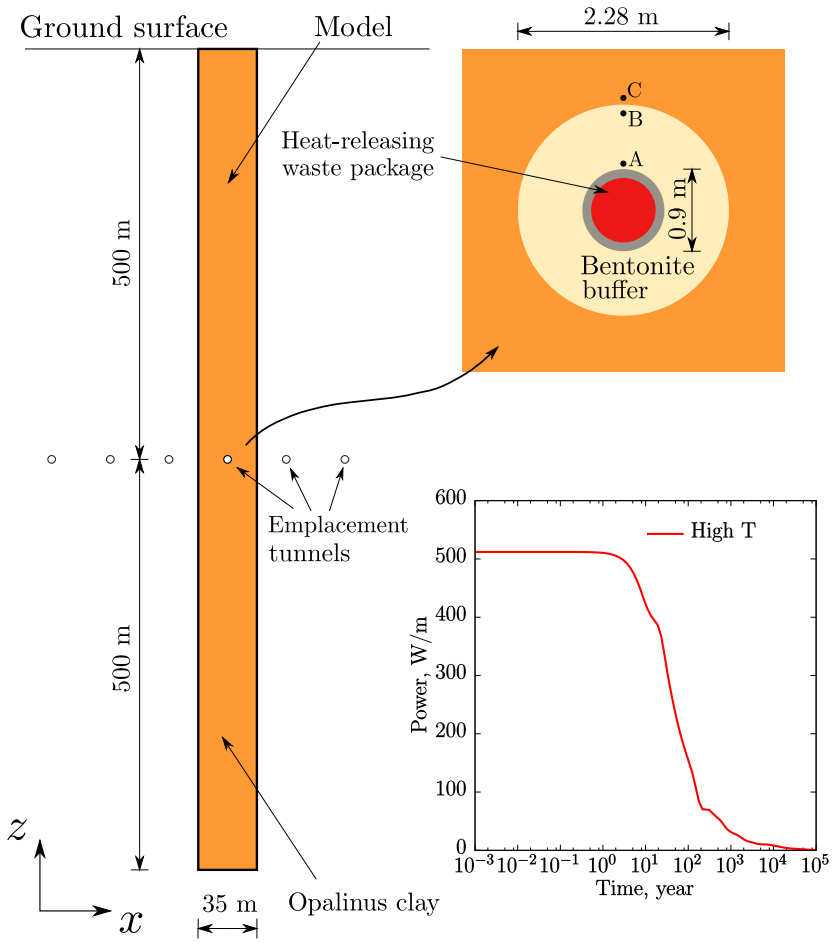

Figure 8: The test example of a horizontal emplacement drift.

lateral boundaries of the model. A free stress boundary is applied at the top of the model domain, and vertical displacements are prevented at the bottom. Constant liquid pressures are applied at both the top and bottom and initially the model domain is in a hydrostatic state. The initial temperature at the top is 11 °C, with a thermal gradient of 27 °C/km, and the initial temperature at the bottom is 38 °C. The model simulation is conducted in a non-isothermal mode with a time-dependent decay heat power [22]. The heat power curve in Figure 8 is scaled from representative decay heat data from the U.S. Department of Energy's Spent Fuel and Waste Science and Technology for Pressurized Water Reactor (PWR) used fuel. This heat load is scaled to represent an equivalent line load, which depends on the assumed spacing between individual waste packages along an emplacement tunnel. The initial heat load right after emplacement corresponds to a thermal power of 520 W/m along the length of the emplacement tunnel.

In this generic case, it is assumed that the host rock properties are representative of Opalinus clay (or argillite) [22, 56] and the backfill is FEBEX bentonite. The bentonite has an initial water saturation of 65% at emplacement and the Opalinus clay is fully saturated. From time zero on, the EBS bentonite undergoes simultaneously re-saturation, heating, chemical alteration, and stress changes. The chemical model considers aqueous complexation, minerals dissolution and precipitation, and cation exchange. Details of these reactions and parameters are given in [57]. In this work, we list the mineralogical information in Table 4 and aqueous composition in Table 5. Table 6 shows the aqueous complexes (secondary species) and 7 shows the cation exchange reactions.Thermal-Hydraulic-Mechanical (THM) properties

are given in Table 8.

Table 4: Initial mineral mass fraction of the FEBEX bentonite and Opalinus clay.

Mineral	FEBEX bentonite	Opalinux Clay
Calcite	0.01	0.11
Dolomite	0.0	0.06
Illite	0.0	0.33
Kaolinite	0.0	0.22
Smectite	0.92	0.042
Chlorite	0.0	0.09
Quartz	0.04	0.13
K-Feldspar	0.01	0.017
Siderite	0.0	0.024
Ankerite	0.0	0.054

Table 5: Pore-water composition of the FEBEX bentonite and Opalinus clay.

	FEBEX bentonite	Opalinux Clay
pH	7.72	7.40
Cl^-	0.16	0.332
${SO_4}^{2-}$	3.20×10^{-2}	1.86×10^{-2}
${HCO_3}^-$	4.1×10^{-4}	5.18×10^{-3}
Ca^{2+}	2.2×10^{-2}	2.26×10^{-2}
Mg^{2+}	2.3×10^{-2}	2.09×10^{-2}
Na^+	0.13	0.276
K^+	1.7×10^{-3}	2.16×10^{-3}
Fe^{2+}	2.06×10^{-8}	3.46×10^{-6}
SiO_2(aq)	1.1×10^{-4}	1.10×10^{-4}
${AlO_2}^-$	1.91×10^{-9}	3.89×10^{-8}
O_2(aq)	2.57×10^{-4}	1.2×10^{-51}

Table 6: Aqueous complexes and their dissociation constants.

Species	Log K (25°C)	Species	Log K (25°)
OH^-	13.99	$MgHCO_3^+$	-1.03
Al^{3+}	-22.88	$CO_2(aq)$	-6.34
$HAlO_2(aq)$	-6.45	CO_3^{2-}	10.33
$NaAlO_2(aq)$	0.75	$CaCO_3(aq)$	7.01
$AlOH^{2+}$	-17.87	KCl(aq)	1.50
$Al(OH)_2^+$	-12.78	$MgCl^+$	0.14
$Al(OH)_3(aq)$	-6.72	$MgSO_4(aq)$	-2.38
$CaCl^+$	0.70	$NaSO_4^-$	-0.81
$CaCl_2(aq)$	0.65	KSO_4^-	-0.88
$CaSO_4(aq)$	-2.10	$NaHSiO_3(aq)$	8.30
NaCl(aq)	0.78	$CaOH^+$	12.85
$FeCl^+$	0.17	NaOH(aq)	14.15
$FeHCO_3^+$	-2.04	$NaCO_3^-$	9.82
$FeCO_3(aq)$	4.88	$NaHCO_3(aq)$	-0.17
$FeCl_4^{2-}$	1.94	$CaHCO_3^+$	-1.04

Table 7: Cation exchange reactions on montmorillonite and illite.

Cation exchange reaction	$K_{Na/M}$
$Na^+ + mon - H = mom - Na + H^+$	1
$Na^+ + mon - K = mom - Na + K^+$	0.0775
$Na^+ + 0.5mon - Ca = mom - Na + 0.5Ca^{2+}$	0.302
$Na^+ + 0.5mon - Mg = mom - Na + Mg^{2+}$	0.302

Table 8: THM parameters.

Parameter	FEBEX bentonite	Opalinus clay
Grain density [kg/m^3]	2700	2700
Porosity, ϕ	0.33	0.162
Saturated permeability [m^2]	2.0×10^{-21}	2.0×10^{-20}
Relative permeability, k_{rl}	$K_{rl} = S^3$	$m = 0.6$, S_{rl}= 0.01
Van Genuchten [1/Pa]	3.3×10^{-8}	6.8×10^{-7}
Van Genuchten, m	0.3	0.6
Pore compressibility [1/Pa]	5.0×10^{-8}	3.2×10^{-9}
Thermal expansion coeff., [1/°C]	1.5×10^{-4}	1.0×10^{-5}
Dry specific heat, [J/kg·°C]	800	860
Thermal conductivity [W/m·°C] dry/wet	1.1/1.5	1.48/1.7
Tortuosity for vapor phase	$\phi^{\frac{1}{3}} S_g^{\frac{10}{3}}$	$\phi^{\frac{1}{3}} S_g^{\frac{10}{3}}$
Bulk modulus, (GPa)	BExM	4.17
Shear modulus, (GPa)	BExM	1.92

4.2. Results and discussions

4.2.1. THC Results

We analyze the evolution of THC behavior looking at two selected locations in the bentonite, one being Point A adjacent the waste canister and the second being Point B near the host rock wall (see locations depicted in Figure 8). Figures 9(a), 9(b), and 9(c) show the temperature changes, the evolution of the pore pressure, and the liquid saturation at Points A and B, respectively. At Point A, near the heat source, the temperature reaches up to 200 °C at around 20 years and then slowly decreases to the ambient temperature, 25 °C after 100,000 years. Point B has a lower maximum temperature, about 170 °C at around 20 years, and a slightly slower initial temperature increase, because of the longer distance to the heater. The liquid saturation at Point A decreases firstly due to evaporation in the vicinity of the waste package and reaches its minimum in about 1 year (Figure 9(c)). Then, the

saturation starts to increase due to water inflow from the surrounding Opalinus clay; Point A reaches full saturation in about 20 years. Point B is close to the host rocks, so it does not go through any dehydration and becomes fully saturated in around 8 years. There is only a slight difference in the pore pressure between Points A and point B (Figure 9(b)). Both start out at the atmospheric pressure (the bentonite is initially at partial saturation). The pore pressure increase is caused by thermal pressurization of the pore water which has limited capability to move away from the buffer due to the low permeability of the bentonite. Since Point B is closer to the heater, the pore pressure at Point B increases earlier than Point A. The pore pressure continuously at both positions increases to a peak of 10.5 MPa at 100 years, after when the fluid pressure begins to dissipate due to cooling effects and no water supply from the canister side. With these effects, the pore pressure reaches a minimum value of 2 MPa at around 30,000 years, and is lower than the ambient pore pressure in surrounding Opalinus clay. Thus, the pore pressure increases again due to the hydration from the outside clay formation. More physical explanation and studies about the similar phenomenon of THM processes in argillaceous host rock can be found in [58, 59].

The chemical behavior of bentonite under high temperature has been studied extensively and the amount of smectite varied greatly depending on the thermal and chemical conditions [40, 48]. The overall reaction of

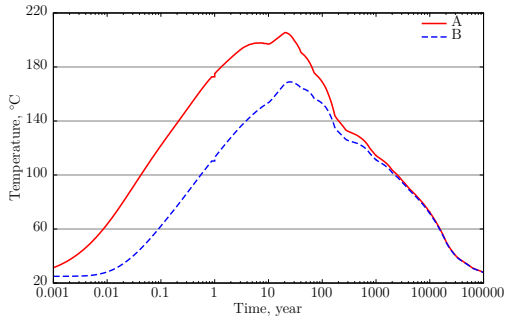

(a) Temperature.

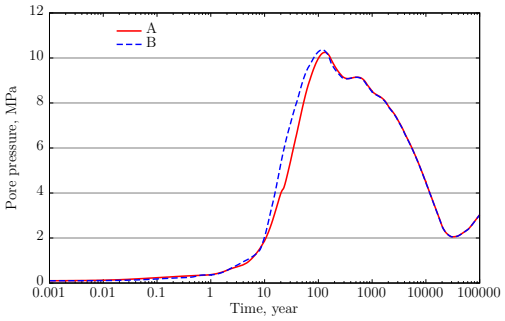

(b) Pore pressure.

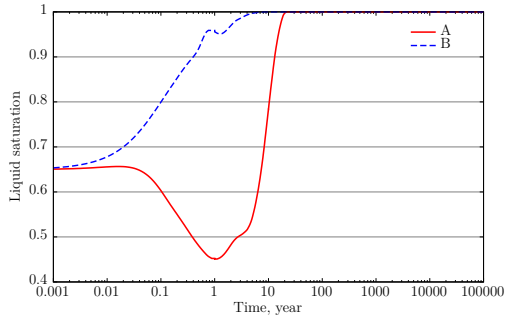

(c) Liquid saturation.

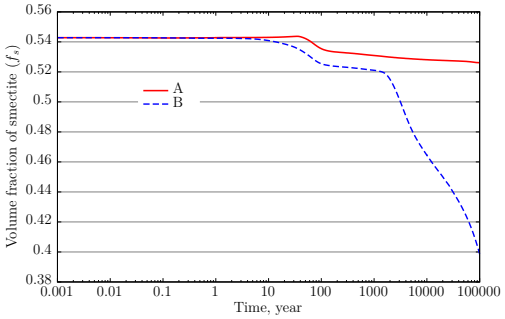

(d) Mass fraction of smectite.

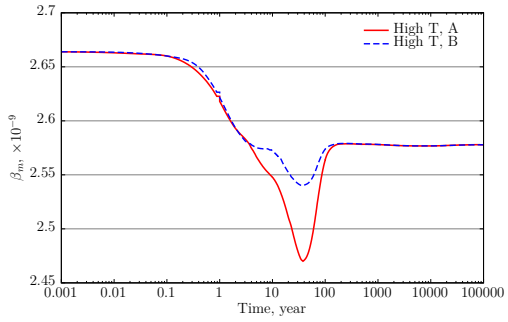

(e) Exchangeable cation concentration, β_m.

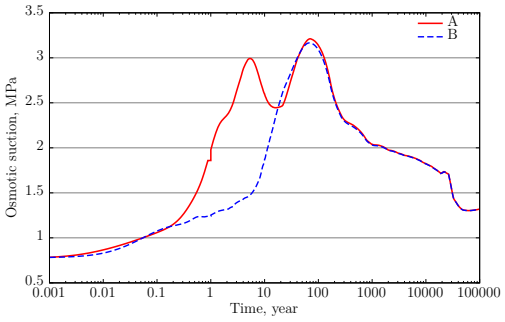

(f) Osmotic suction.

Figure 9: Simulation results of THMC evolution at Points A and B within FEBEX bentonite.

illitization can be written as:

$$\text{Smectite} + 0.52\text{H}^+ + 0.63\text{AlO}_2^- + 0.6\text{K}^+ = \text{Illite} + 0.26\text{H}_2\text{O} + 0.08\text{Mg}^{2+} + 0.33\text{Na}^+ + 0.5\text{SiO}_2(\text{aq}) \quad (15)$$

Because the pore-water in argillite has higher K concentration than that in bentonite, the infiltration of water from argillite into the bentonite raise the concentration of K in the pore water of bentonite and trigger the above reaction, i.e. the dissolution of smectite and precipitation of illite. In addition, the dissolution of K-plagioclase also supplied K for the proceeding of the illitization reaction.

Our model shows dissolution of smectite, in particular in the bentonite region close to the host rock (Figure 9(d)). The mass fraction of smectite, f_s, decreases from 92% to 89.1% at Point A, and to 67.6% at Point B.

Figure 9(e) shows the evolution of β_m at Points A and B. In the current model, β_m depends on the concentration of the exchangeable cations, Na^+, K^+, Ca^{2+} and Mg^{2+}. The evolution of exchangeable cation concentration is displayed in Figure 10. The initial value of β_m^i was calibrated in Section 3.3, and the model predicts a reduction of β_m from 2.664×10^{-9} to 2.48×10^{-9} at Point A and from 2.664×10^{-9} to 2.538×10^{-9} at Point B in the first 40 years (Figure 9(e)), which is mainly due to exchangeable Mg^{2+} being replaced by exchangeable Na^+ (Figure 10). After that, both β_m values recover back to 2.58×10^{-9}, because the reduction of Ca^{2+} is compensated by the accumulation of Na^+. The increases of β_m indicates the strengthening of the exchangeability of cations in the interlayer space of bentonite, resulting in that the adsorption of water is enhanced, and, in turn, the swelling of

bentonite increases. The impact will be that the degree of swelling stress increment due to the change of exchangeable cations could be suppressed during the first 40 years due to the initial drop of β_m, but should then rise since β_m bounces back.

Figure 9(f) shows the evolution of osmotic suction at Points A and B. An increase of osmotic suction indicates the water movement in porous medium is suppressed, as a result of that it tends to reduce the swelling of bentonite, whereas a decrease of osmotic suction enhances swelling. For Point A, the osmotic suction shows a two-peak behavior, with one peak of about 3 MPa after 3 years and the second at 3.25 MPa after 80 years, then starts to decrease until the end of simulation. At Point B, the peak magnitude 3.25 MPa is reached at around 80 years. The osmotic suction reduces to 1.3 MPa at both points by the end of the simulation.

4.2.2. Mechanical results

To better understand the transient mechanical behavior of the swelling clay and how the BExM represents this behavior, we discuss the evolution of both macro- and micro-structures here. We start by analyzing the stress path at Points A and B as predicted with the BExM. Figure 11 presents the stress path in the 3D q-p-s_m space and its corresponding projection onto the p-s_m plane. Figures 12(a) and 12(b) display the 2D stress path again together with the evolution of p_0 in terms of suction. Figures 12(c) and 12(d) present the changes of void ratio (macro, micro and total) in terms of suction. Figures 12(e) and 12(f) depict the evolution of the values of the

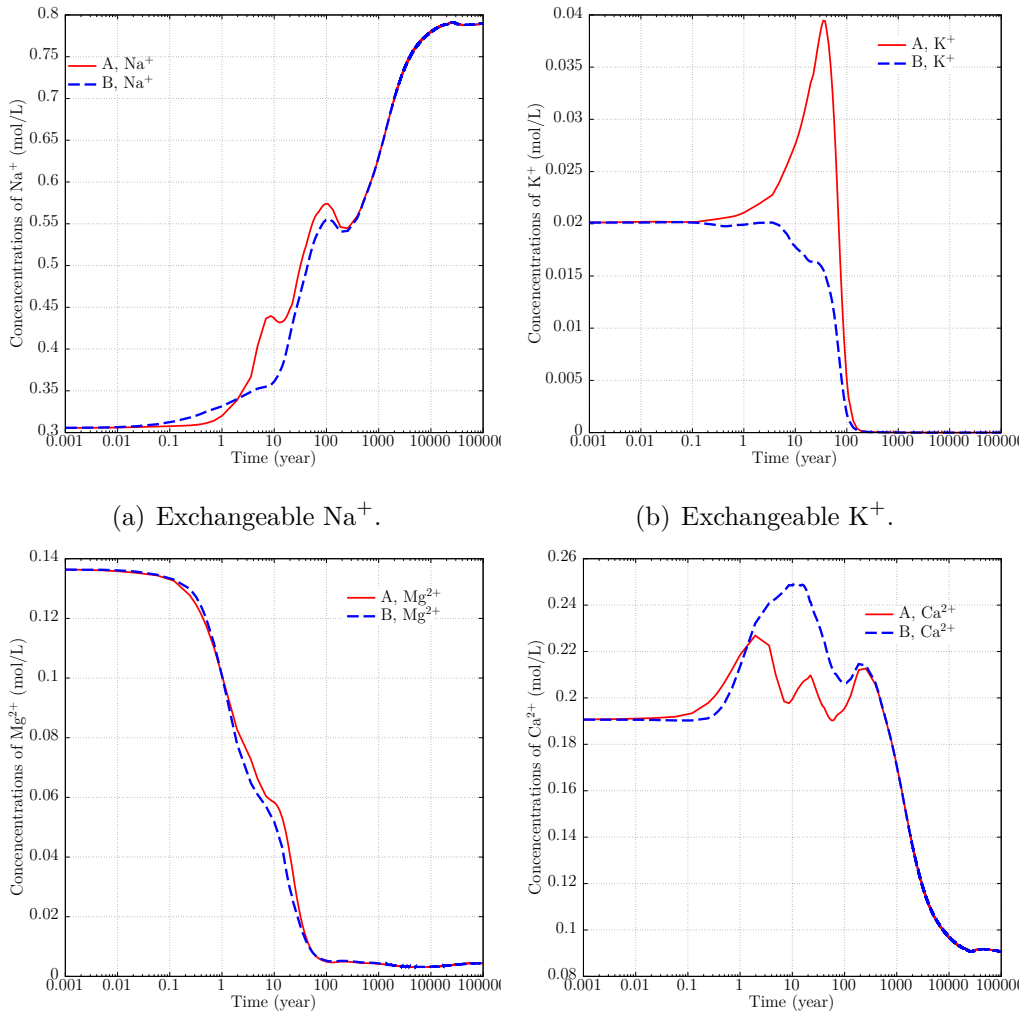

(a) Exchangeable Na^+.

(b) Exchangeable K^+.

(c) Exchangeable Mg^{2+}.

(d) Exchangeable Ca^{2+}.

Figure 10: Simulated concentration of exchangeable cations at Points A and B within FEBEX bentonite.

interaction functions during the various stages of the analysis.

Very early on after waste and bentonite emplacement, since thermal effects are not strong yet and the temperature is still relatively low, the bentonite at Point A starts to swell, and the interaction function f_{is} is triggered as Figure 12(e) shows. Later when the temperature rises beyond 100°C, the bentonite at Point A is subjected to drying—the liquid saturation decreases and the suction increases, activating a MC mechanism at the micro-scale. The interaction function f_{ic} is positive in Figure 12(e) and induces small compressive plastic macro-structural deformation. Moreover, the increase of the mean net stress due to the confinement accumulation from the external zones of the buffer and the host rock leads to contraction of the macro-structure. As a result, the macro-structure is densified, as shown by the growth of p_0 in Figure 12(a), and the reduction of total void ratio in Figure 12(c). After about one year, the bentonite at Point A returns to hydration, as fluids from the host rock migrate towards this location: the liquid saturation increases again, as shown in Figure 9(c), and suction subsequently decreases, resulting in swelling of bentonite and activation of the interaction function f_{is}. As Figure 12(e) displays, f_{is} is positive and induces tensile plastic macro-structural strain, but then it changes to negative and, consequently, induces compressive plastic strain. The mean net stress still increases during this stage, which results in macro-structural contraction. However, at this stage, the temperature increases above 180 °C (Figure 9(a)), inducing significant thermal expansion at the macro-scale and causing a macro-void ratio increase. The total void ratio increases during this phase (Figure 12(c)), while p_0 follows a complicated increase/decrease path until it becomes steady when the

bentonite is fully saturated (Figures 12(a)). After full saturation, the state variables at Point A do not change much, except the interaction function continues to switch between f_{ic} and f_{is} paths due to numerical fluctuations in the computation. In Figure 9(a), the final LC curve is to the right of the initial one, indicating the increment of the elastic domain, and the hardening of the material.

Point B is close to the host rock and the bentonite here undergoes hydration from the very beginning, so a different behavior is observed in Figure 12(b), 12(d) and 12(f). The initial state at Point B is under compression due to the confinement from the host rock. Thus, at the beginning, the simulated results in Figure 12(d) show a slight contraction at the macro-scale while the total and the macro-void ratio decrease. The micro-structure is also under compression, which is implied by the interaction function following a f_{ic} path with MC mechanism in Figure 12(f). As Figure9(c) displays, early hydration at Point B leads to increased liquid saturation and reduced suction. As a result of these facts, the bentonite swells and a MS mechanism is activated. The evolution of f_{is} at point B is similar to that at Point A during the wetting phase as the system evolves to full saturation. Firstly, f_{is} is positive in Figure 12(f) and induces tensile plastic macro-structural strain, then it changes to negative and induces compressive plastic strain. Later, thermal expansion at the macro-scale also happens when this position reaches full saturation condition, causing a slight increase of macro-void ratio (Figure 12(d)). The total void ratio increases during this phase mainly due to contributions from micro-structural swelling. During this phase, some suction increases occur as well, so the interaction function changes to a MC

mechanism with $f_{ic} > 0$ for a short period, then it goes back to a MS path (Figure 12(f)). This implies large micro-structural swelling due to the strong reduction of micro-structural effective stresses. After 100 years, the macro-structure contracts again mainly due to the accumulation of effective stresses at the macro-scale when liquid pressure dissipates. This fact causes a reduction of the macro and total void ratio. In Figure 12(b), the final LC curve moves to the right, which indicates the growth of the elastic domain, and hardening of the material.

Usually, swelling stress is associated with effective stress when a soil sample is subjected to hydration. In Figure 13, we present the mean effective/net stress, i.e., the mean net stress for unsaturated bentonite and the mean effective stress for fully saturated bentonite during the simulation (marked as "W C-M") to illustrate the accumulation of swelling stress in the solid skeleton of the bentonite. At Point A, the mean effective/net stress is about 5.7 MPa at peak, around 20 years after emplacement. The reason for the increase of peak swelling stress is that an initial drying of the bentonite enhances the peak swelling pressure at full saturation, which is similar to the initial desaturation process (path A-B in Figure 3(b)) in test S5 increases the swelling deformation during the hydration stage (path B-D in Figure 3(b)). Additionally, thermal expansion due to heating also contributes to the stress accumulation. As the state of bentonite changes from unsaturated condition to fully saturated, effective stresses are plotted instead of net stresses. The effective stress decreases after the full saturation due to the fact that pore

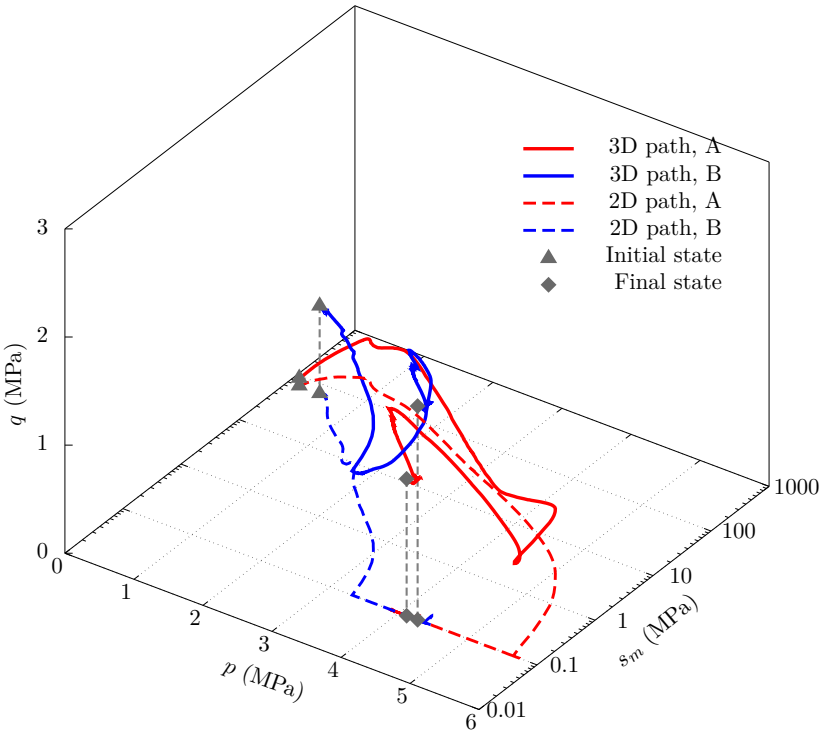

Figure 11: Stress path at Points A and B in the 3D q-p-s_m space.

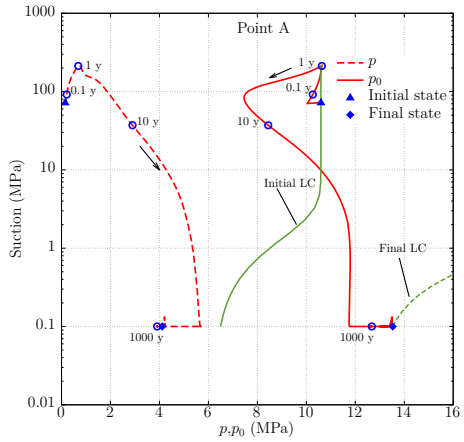

(a) Stress path of Point A on p-s_m plane.

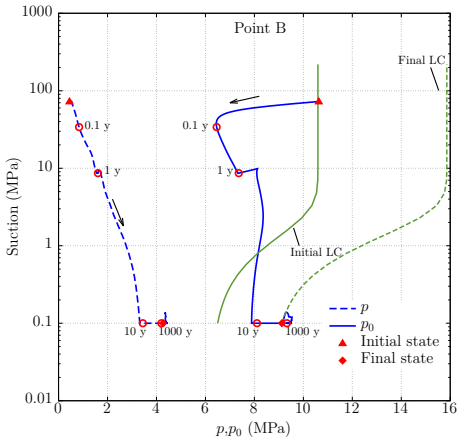

(b) Stress path of Point B on p-s_m plane.

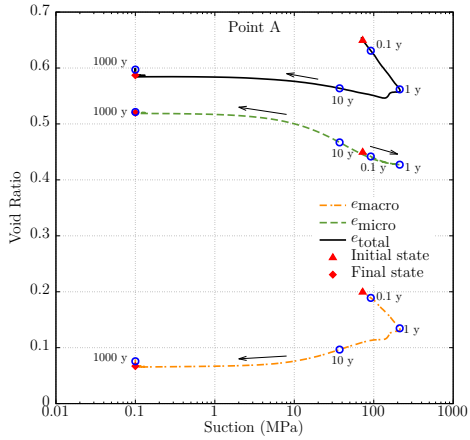

(c) Void ratio evolution at Point A.

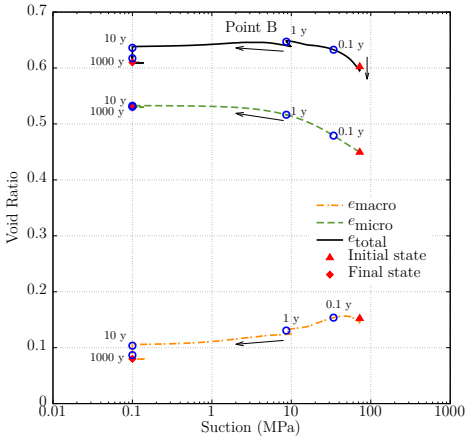

(d) Void ratio evolution at Point B.

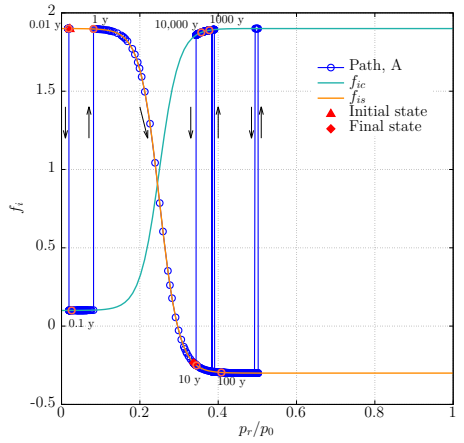

(e) Interaction function at Point A.

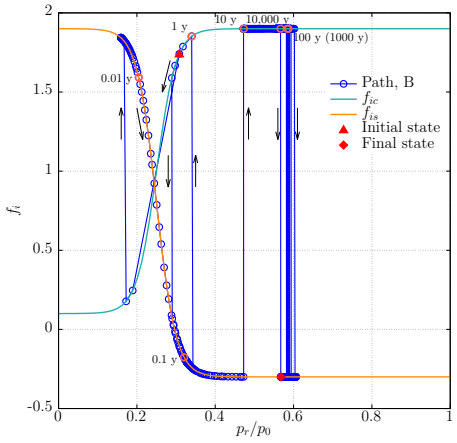

(f) Interaction function at Point B.

Figure 12: Simulation results of bentonite behavior at Points A and B within FEBEX bentonite. LC is the Loading-Collapse curve or the yield locus for the macro-structure.

pressure increases (Figure 9(b)) and stress redistribution occurs. After 100 years, the effective stress starts to increases again, which is due to the decline of osmotic suction and a strong pore pressure reduction. It should be noticed that no volumetric collapse happens at Point A since the material does not reach the LC curve, as indicated in Figure 12(a). The key variables affecting the LC curve are the net mean yield stress at full saturation, p_0^*, and macro-structural stiffness parameters, $\lambda(s_m)$ and κ, which are obtained from laboratory experiments but depend on the compaction status of the samples.

At Point B, the peak stress at full saturation is 1.2 MPa lower than the stress at Point A due to the fast saturation process and strong confinement induced by strong thermal stresses. This finding is similar to the discovery in test S1, in which an initial loading process (path B-C in Figure 3(b)) suppresses the swelling during the hydration process (path C-E in Figure 3(b)). However, later, the stress recovers to about 4.2 MPa around 40,000 years.

Figure 13 also presents another case that was simulated without C-M coupling (marked as "W/o C-M"), meaning the mass fraction of smectite, exchangeable cation concentration, and osmotic suction are all kept constant as the initial input. By accounting for C-M coupling, the peak stress at Point A is 0.6 MPa lower than the case without C-M coupling, while the peak stress at Point B is only 0.2 MPa lower, which is mainly caused by the different cation exchange at the time when stress peaks, as manifested by the β_m in Figure 9(e). For the final recovered stress, both Points A and B exhibit lower stress values if C-M coupling is considered, indicating that chemical effects reduce the final effective/net stress in the bentonite buffer. The magnitude

of stress reduction at Point A is larger than that at Point B, resulting in a lower final effective stress at Point A (Figure 13). However, the reduction in stress magnitude is less than 1 MPa.

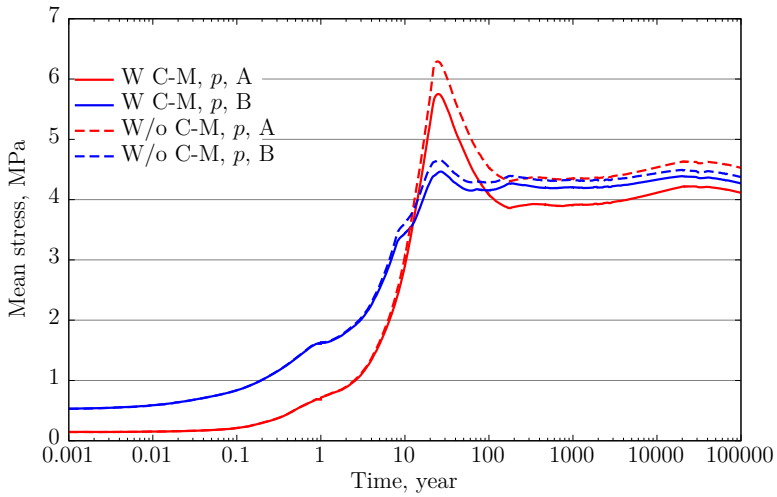

Figure 13: Simulation results of stress at Points A and B within FEBEX bentonite.

5. Conclusions

In this paper, we have used a coupled THMC model with the newly implemented dual-structural BExM to study the behavior of bentonite exposed to heating and hydration. In contrast to constitutive models for unsaturated soils that usually only account for macro-structural behavior, the incorporation of micro-structure effects in the BExM allows for improved prediction of bentonite behavior. In the BExM, swelling can occur at the micro-scale on the basis of the stress path and suction changes, and this will cause the swelling micro-structure to invade into the macro-porosity, the quantity of which depends on the mechanical confinement and load level at the

macro-scale. The interaction between micro- and macro-structures provides a physical-based approach to understand and describe the complicated behavior of expansive clay with soil fabric effects as observed in experiments.

The BExM constitution has been formulated in the framework of elasto-plasticity and we implemented it in the finite difference simulator TOUGHREACT-FLAC3D. We conducted one benchmark case to verify the correctness of model implementation, a series of experiments with a combination of loading paths on FEBEX bentonite. In this case, we achieved a good agreement between model results and experimental data. To account for the effects of chemical reaction, we utilized a C-M coupling approach, in which three types of chemical changes that affect mechanical behavior were incorporated through BExM: (1) the evolution of mass fraction of smectite, (2) the exchangeable cation concentration, and (3) the ionic strength via osmotic suction. With the C-M coupling, we successfully calibrated the various parameters required for BExM against laboratory experiments where FEBEX bentonite was exposed to solutions of various salinity.

Finally, we conducted a coupled THMC simulation with BExM for a hypothetical bentonite-backfilled nuclear waste repository with a maximum temperature of 200 °C at the canister-bentonite interface, focusing on the effect of chemical changes on swelling stress and stress path. Our model shows a complex transient behavior in the bentonite with complicated interaction between thermal-hydrological-mechanical and chemical processes and different state variable evolution depending on the location (i.e., near the heater vs near the host rock boundary). Microscopically, the model predicts a decrease of the mass fraction of smectite in solid bentonite due to dissolution,

an increase in osmotic suction, and an increase in exchangeable Na^+ in the interlayer space. The combination of these chemical changes reduces the effective/net stress in the bentonite buffer under heated condition. Simulation results also show that: (1) the micro-structure swells with suction reduction and induces plastic macro-structural deformation following the path of interaction function; (2) the macro-structure hardens and becomes denser; (3) the initial saturated pre-consolidation pressure, a parameter dependent on the stress history, strongly affects the mechanical evolution of bentonite; (4) the net/effective stress increases initially to peak at around 20 years, then reduces and becomes stable; (5) the area near the heat-emanating waste canister experiences a higher stress peak than the area near the host rock because of the drying and thermal expansion occurring at the early times, but the final stress at 100,000 years is lower than the area near the host rock due to long-term chemical effects. We conclude that the model is able to simulate a complicated THMC demonstration case for bentonite behavior over a long time period of up to 100,000 years, using a physics-based multi-scale approach to represent the dual-structure nature of bentonite.

Appendix A. The parameters and equations of BExM [15, 60, 28]

Appendix A.1. Nomenclature

e_m	macro-structural void ratio	e_M	macro-structural void ratio
f_i	interaction functions	f_{ic}	Micro-structural Compression (MC) path
f_{is}	Micro-structural Swelling (MS) path	f_{ic0}, ... , f_{is0}, ...	constants for interaction functions
f_{LC}	yield surface for the macro-struture	g_{LC}	plastic potential of a non-associated flow rule
G_M	macro-structural shear modulus	k_s	an empirical material constant
K_m	micro-structural bulk modulus	K_M	macro-structural bulk modulus
K_s	macro-structural bulk modulus for changes in matric suction	K_T	macro-structural bulk modulus associated with the temperature change
M	slope of the critical state	p	mean stress of $\boldsymbol{\sigma}$
$\hat{p}$	effective stress	p''	mean net stress
p_{atm}	atmospheric pressure	p_c	net mean yield stress at the reference matric suction
p_g	gas pressure	p_l	liquid pressure
p_r	anisotropic stress state projected from the anisotropic stress state	p_s	dependence of shear strength on matric suction
p_ϕ	pore pressure	p_0	apparent unsaturated isotropic preconsolidation pressure
p_0^*	net mean yield stress at full saturation	q	deviatoric stress
r	a constant defining the maximum stiffness of the soil	s_m	matric suction
s_o	osmotic suction	s_t	total suction
α	a parameter to determine non-associated plastic strains	α_m, β_m	compressibility parameters for the micro-structure
α_0	volumetric thermal expansion coefficient	ε_{qm}^e	micro-structural strains due to deviatoric stress

ε^e_{qM}	elastic deviatoric strain at the macro-scale	ε^e_{vm}	micro-structural strains due to mean effective stress
ε^e_{vM}	elastic volumetric strain at the macro-scale	ε^p_v	total plastic volumetric strains
ε^p_{vLC}	plastic strains from the macro-structural	$\varepsilon^p_{v\beta}$	macro-structural plastic strains
ζ	parameter controlling the rate of increase of macro-structural soil stiffness with suction	κ	macro-structural elastic stiffness parameters for changes in mean stress.
κ_s	macro-structural elastic stiffness parameters for changes in matric suction	λ	macro-structural compressibility parameter for changes in net mean stress for virgin states of soil at matric suction
$\mathrm{d}\lambda$	plastic multiplier		

Appendix A.2. Equations

$$\boldsymbol{\sigma} = \boldsymbol{\sigma}^{total} - p_\phi \mathbf{I}, \tag{A.1}$$

$$p_\phi = \max(p_l, p_g). \tag{A.2}$$

$$\begin{aligned} p &= p\text{"} \quad \text{if } s_l < 1; \\ p &= \hat{p} \quad \text{if } s_l = 1. \end{aligned} \tag{A.3}$$

$$f_{LC} = q^2 - M^2 (p + p_s)(p_0 - p), \tag{A.4}$$

$$p_s = k_s s_m \tag{A.5}$$

$$p_o = p_c \left(\frac{p_0^*}{p_c} \right)^{[\lambda(0)-\kappa]/[\lambda(s_m)-\kappa]}, \tag{A.6}$$

$$\lambda(s_m) = \lambda(0) \left[r + (1 - r) \exp(-\zeta s_m) \right] \tag{A.7}$$

$$\mathrm{d}\varepsilon^e_{vM} = \frac{1}{K_M} \mathrm{d}p + \frac{1}{K_s} \mathrm{d}s_m + \frac{1}{K_T} \mathrm{d}T, \tag{A.8}$$

$$K_M = \frac{(1+e_M)p}{\kappa}, \tag{A.9}$$

$$K_s = \frac{(1+e_M)(s_m + p_{\text{atm}})}{\kappa_s}, \tag{A.10}$$

$$K_T = \frac{1}{\alpha_0}, \tag{A.11}$$

$$\mathrm{d}\varepsilon^e_{qM} = \frac{1}{3G_M}\mathrm{d}q, \tag{A.12}$$

$$G_M = \frac{3(1-2\nu)}{2(1+\nu)}K_M. \tag{A.13}$$

$$g_{LC} = \alpha q^2 - M^2\left(p + p_s\right)\left(p_0 - p\right), \tag{A.14}$$

$$\mathrm{d}\varepsilon^p_{vLC} = \mathrm{d}\lambda\frac{\partial g_{LC}}{\partial p}, \tag{A.15}$$

$$\mathrm{d}\varepsilon^p_{qLC} = \mathrm{d}\lambda\frac{\partial g_{LC}}{\partial q}, \tag{A.16}$$

$$\hat{p} = p + s_t, \tag{A.17}$$

$$s_t = s_m + s_o \tag{A.18}$$

$$\mathrm{d}\varepsilon^e_{vm} = \frac{1}{K_m}\mathrm{d}\hat{p}, \tag{A.19}$$

$$\mathrm{d}\varepsilon^e_{qm} = \frac{1}{3G_m}\mathrm{d}q, \tag{A.20}$$

$$K_m = \frac{e^{\alpha_m \hat{p}}}{\beta_m}, \tag{A.21}$$

$$\mathrm{d}\varepsilon^p_{v\beta} = f_i\,\mathrm{d}\varepsilon^e_{vm}, \tag{A.22}$$

$$\begin{aligned}
&\dot{\hat{p}} > 0 \Rightarrow \text{Micro-structural Compression (MC) path} : f_i = f_{ic};\\
&\dot{\hat{p}} < 0 \Rightarrow \text{Micro-structural Swelling (MS) path} : f_i = f_{is}.
\end{aligned} \tag{A.23}$$

$$\begin{aligned}
f_{ic} =& f_{ic0} + f_{ic1}\tanh\left[f_{ic2}\left(\frac{p_r}{p_0} - f_{ic3}\right)\right],\\
f_{is} =& f_{is0} - f_{is1}\tanh\left[f_{is2}\left(\frac{p_r}{p_0} - f_{is3}\right)\right],
\end{aligned} \tag{A.24}$$

$$p_r = p + \frac{q^2}{M^2\,(p + p_s)}. \tag{A.25}$$

$$\mathrm{d}\varepsilon_v^p = \mathrm{d}\varepsilon_{vLC}^p + \mathrm{d}\varepsilon_{v\beta}^p. \tag{A.26}$$

$$\frac{\mathrm{d}p_0^*}{p_0^*} = \frac{(1+e)\mathrm{d}\varepsilon_v^p}{\lambda(0) - \kappa}. \tag{A.27}$$

Acknowledgments

Funding for this work was provided by the Spent Fuel and Waste Science and Technology, Office of Nuclear Energy, of the U.S. Department of Energy under Contract Number DE-AC02-05CH11231 with Lawrence Berkeley National Laboratory.

References

[1] Alonso, E., Alcoverro, J., Coste, F., Malinsky, L., Merrien-Soukatchoff, V., Kadiri, I., et al. The FEBEX benchmark test: case definition and comparison of modelling approaches. International Journal of Rock Mechanics and Mining Sciences 2005;42(5–6):611–638. doi: https://doi.org/10.1016/j.ijrmms.2005.03.004.

[2] Garitte, B., Shao, H., Wang, X.R., Nguyen, T.S., Li, Z., Rutqvist, J., et al. Evaluation of the predictive capability of coupled thermo-hydro-mechanical models for a heated bentonite/clay system (HE-E) in the Mont Terri Rock Laboratory. Environmental Earth Sciences 2017;76:64. doi:https://doi.org/10.1007/s12665-016-6367-x.

[3] Alonso, E., Hoffmann, C.. Modelling the field behaviour of a granular expansive barrier. Physics and Chemistry of the Earth, Parts A/B/C 2007;32(8–14):850–865. doi:https://doi.org/10.1016/j.pce.2006.04.039.

[4] Tripathy, S., Subba Rao, K., Fredlund, D.. Water content – void ratio swell–shrink paths of compacted expansive soils. Canadian Geotechnical Journal 2002;39(4):938–959. doi:https://doi.org/10.1139/t02-022.

[5] Villar, M.. Investigation of the behaviour of bentonite by means of suction–controlled oedometer tests. Engineering Geology 1999;54(1–2):67–73. doi:https://doi.org/10.1016/S0013-7952(99)00062-9.

[6] Komine, H., Ogata, N.. Experimental study on swelling characteristics of compacted bentonite. Canadian Geotechnical Journal 1994;31(4):478–490. doi:https://doi.org/10.1139/t94-057.

[7] Komine, H., Ogata, N.. Prediction for swelling characteristics of compacted bentonite. Canadian Geotechnical Journal 1996;33(1):11–22. doi:https://doi.org/10.1139/t96-021.

[8] Stawiński, J., Wierzchoś, J., Garcia-Gonzalez, M.T.. Influence of Calcium and Sodium concentration on the microstructure of bentonite and Kaolin. Clays and Clay Minerals 1990;38(6):617–622. doi:https://doi.org/10.1346/CCMN.1990.0380607.

[9] Saiyouri, N., Hicher, P.Y., Tessier, D.. Microstructural approach and transfer water modelling in highly compacted unsaturated swelling clays. Mechanics of Cohesive-Frictional Materials 2000;5(1):41–60. doi:10.1002/(SICI)1099-1484(200001)5:1<41::AID-CFM75>3.0.CO;2-N.

[10] Dixon, D., Graham, J., Gray, M.N.. Hydraulic conductivity of clays in confined tests under low hydraulic gradients. Canadian Geotechnical Journal 1999;36(5):815–825. doi:https://doi.org/10.1139/t99-057.

[11] Delage, P., Marcial, D., Cui, Y.J., Ruiz, X.. Ageing effects in a compacted bentonite: a microstructure approach. Géotechnique 2006;56(5):291–304. doi:https://doi.org/10.1680/geot.2006.56.5.291.

[12] Zhou, A., Sheng, D.. An advanced hydro-mechanical constitutive model for unsaturated soils with different initial densities. Computers and Geotechnics 2015;63:46–66. doi: https://doi.org/10.1016/j.compgeo.2014.07.017.

[13] Zhou, A.N., Sheng, D., Sloan, S.W., Gens, A.. Interpretation of unsaturated soil behaviour in the stress–saturation space II: Constitutive relationships and validations. Computers and Geotechnics 2012;43:111–123. doi:https://doi.org/10.1016/j.compgeo.2012.02.009.

[14] Alonso, E.E., Gens, A., Josa, A.. A constitutive model for partially saturated soils. Géotechnique 1990;40(3):405–430. doi: https://doi.org/10.1680/geot.1990.40.3.405.

[15] Gens, A., Sánchez, M., Sheng, D.. On constitutive modelling of unsaturated soils. Acta Geotechnica 2006;1(3):137–147. doi: https://doi.org/10.1007/s11440-006-0013-9.

[16] Laloui, L., Cekerevac, C.. Thermo-plasticity of clays: An isotropic yield mechanism. Computers and Geotechnics 2003;30(8):649–660. doi: https://doi.org/10.1016/j.compgeo.2003.09.001.

[17] Cui, W., Potts, D.M., Zdravković, L., Gawecka, K.A., Taborda, D.M.. An alternative coupled thermo-hydro-mechanical finite element formulation for fully saturated soils. Computers and Geotechnics 2018;94:22–30. doi:https://doi.org/10.1016/j.compgeo.2017.08.011.

[18] Bellia, Z., Ghembaza, M.S., Belal, T.. A thermo-hydro-mechanical model of unsaturated soils based on bounding surface plasticity. Computers and Geotechnics 2015;69:58–69. doi:https://doi.org/10.1016/j.compgeo.2015.04.020.

[19] François, B., Laloui, L.. ACMEG-TS: A constitutive model for unsaturated soils under non-isothermal conditions. International Journal for Numerical and Analytical Methods in Geomechanics 2008;32(16):1955–1988. doi:https://doi.org/10.1002/nag.712.

[20] Gens, A., Sánchez, M., Guimarães, L., Alonso, E.E., Lloret, A., Olivella, S., et al. A full-scale in situ heating test for high-level nuclear waste disposal: observations, analysis and interpretation. Géotechnique 2009;59(4):377–399. doi:https://doi.org/10.1680/geot.2009.59.4.377.

[21] Rutqvist, J., Ijiri, Y., Yamamoto, H.. Implementation of the Barcelona Basic Model into TOUGH–FLAC for simulations of the geomechanical behavior of unsaturated soils. Computers & Geosciences 2011;37(6):751–762. doi:https://doi.org/10.1016/j.cageo.2010.10.011.

[22] Rutqvist, J., Zheng, L., Chen, F., Liu, H., Birkholzer, J.. Modeling of coupled thermo-hydro-mechanical processes with links to geochemistry associated with bentonite-backfilled repository tunnels in clay

formations. Rock Mechanics and Rock Engineering 2014;47(1):167–186. doi:https://doi.org/10.1007/s00603-013-0375-x.

[23] Abed, A.A., Sołowski, W.T.. A study on how to couple thermo-hydro-mechanical behaviour of unsaturated soils: Physical equations, numerical implementation and examples. Computers and Geotechnics 2017;92:132–155. doi:https://doi.org/10.1016/j.compgeo.2017.07.021.

[24] Kristensson, O., Åkesson, M.. Mechanical modeling of MX-80 – quick tools for BBM parameter analysis. Physics and Chemistry of the Earth, Parts A/B/C 2008;33(1):S508–S515. doi:https://doi.org/10.1016/j.pce.2008.10.003.

[25] Åkesson, M., Kristensson, O.. Mechanical modeling of MX-80 – development of constitutive laws. Physics and Chemistry of the Earth, Parts A/B/C 2008;33(1):S504–S507. doi:https://doi.org/10.1016/j.pce.2008.10.014.

[26] Dupray, F., François, B., Laloui, L.. Analysis of the FEBEX multi-barrier system including thermoplasticity of unsaturated bentonite. International Journal for Numerical and Analytical Methods in Geomechanics 2013;37(4):399–422. doi:https://doi.org/10.1002/nag.1103.

[27] Sánchez, M., Gens, A., Guimarães, L., Olivella, S.. Implementation algorithm of a generalised plasticity model for swelling clays. Computers and Geotechnics 2008;35(6):860–871. doi:https://doi.org/10.1016/j.compgeo.2008.08.004.

[28] Sánchez, M., Gens, A., Guimarães, L., Olivella, S.. A double structure generalized plasticity model for expansive materials. International Journal for Numerical and Analytical Methods in Geomechanics 2005;29(8):751–787. doi:https://doi.org/10.1002/nag.434.

[29] Sánchez, M., Gens, A., Olivella, S.. THM analysis of a large-scale heating test incorporating material fabric changes. International Journal for Numerical and Analytical Methods in Geomechanics 2012;36(4):391–421. doi:https://doi.org/10.1002/nag.1011.

[30] Vilarrasa, V., Rutqvist, J., Blanco-Martin, L., Birkholzer, J.. Use of a dual-structure constitutive model for predicting the long-term behavior of an expansive clay buffer in a nuclear waste repository. International Journal of Geomechanics 2016;16(6):D4015005. doi:https://doi.org/10.1061/(ASCE)GM.1943-5622.0000603.

[31] Rutqvist, J., Barr, D., Birkholzer, J.T., Chijimatsu, M., Kolditz, O., Liu, Q., et al. Results from an international simulation study on coupled thermal, hydrological, and mechanical processes near geological nuclear waste repositories. Nuclear Technology 2008;163(1):101–109. doi:https://doi.org/10.13182/NT08-A3974.

[32] Ulm, F.J., Coussy, O.. Couplings in early-age concrete: From material modeling to structural design. International Journal of Solids and Structures 1998;35(31–32):4295–4311. doi:https://doi.org/10.1016/S0020-7683(97)00317-X.

[33] Coussy, O., Ulm, F.J.. Creep and plasticity due to chemo-mechanical

couplings. Archive of Applied Mechanics 1996;66(8):523–535. doi: https://doi.org/10.1007/BF00808142.

[34] Coussy, O.. Poromechanics. John Wiley & Sons; 2004. doi: 10.1002/0470092718.

[35] Yin, S., Towler, B.F., Dusseault, M.B., Rothenburg, L.. Fully coupled THMC modeling of wellbore stability with thermal and solute convection considered. Transport in Porous Media 2010;84(3):773–798. doi:https://doi.org/10.1007/s11242-010-9540-9.

[36] Yin, S., Dusseault, M.B., Rothenburg, L.. Coupled THMC modeling of CO_2 injection by finite element methods. Journal of Petroleum Science and Engineering 2011;80(1):53–60. doi: https://doi.org/10.1016/j.petrol.2011.10.008.

[37] Sherwood, J.D.. Biot poroelasticity of a chemically active shale. Proceedings of the Royal Society of London Series A: Mathematical and Physical Sciences 1993;440(1909):365–377. doi: https://doi.org/10.1098/rspa.1993.0021.

[38] Taron, J., Elsworth, D., Min, K.B.. Numerical simulation of thermal-hydrologic-mechanical-chemical processes in deformable, fractured porous media. International Journal of Rock Mechanics & Mining Sciences 2009;46(5):842–854. doi: https://doi.org/10.1016/j.ijrmms.2009.01.008.

[39] Kim, J., Sonnenthal, E., Rutqvist, J.. A sequential implicit algorithm of chemo-thermo-poro-mechanics for fractured geother-

mal reservoirs. Computers & Geosciences 2015;76:59–71. doi: https://doi.org/10.1016/j.cageo.2014.11.009.

[40] Zheng, L., Rutqvist, J., Xu, H., Birkholzer, J.T.. Coupled THMC models for bentonite in an argillite repository for nuclear waste: Illitization and its effect on swelling stress under high temperature. Engineering Geology 2017;230:118–129. doi: https://doi.org/10.1016/j.enggeo.2017.10.002.

[41] Guimarães, L., Gens, A., Sánchez, M., Olivella, S.. A chemo-mechanical constitutive model accounting for cation exchange in expansive clays. Géotechnique 2013;63(3):221–234. doi: https://doi.org/10.1680/geot.SIP13.P.012.

[42] Loret, B., Hueckel, T., Gajo, A.. Chemo-mechanical coupling in saturated porous media: elastic–plastic behaviour of homoionic expansive clays. International Journal of Solids and Structures 2002;39(10):2773–2806. doi:https://doi.org/10.1016/S0020-7683(02)00151-8.

[43] Lei, X., Wong, H., Fabbri, A., Limam, A., Cheng, Y.. A thermo-chemo-electro-mechanical framework of unsaturated expansive clays. Computers and Geotechnics 2014;62:175–192. doi: https://doi.org/10.1016/j.compgeo.2014.07.004.

[44] Lei, X., Wong, H., Fabbri, A., Limam, A., Cheng, Y.. A chemo-elastic-plastic model for unsaturated expansive clays. International Journal of Solids and Structures 2016;88-89:354–378. doi: https://doi.org/10.1016/j.ijsolstr.2016.01.008.

[45] Zheng, L., Xu, H., Rutqvist, J., Reagan, M., Birkholzer, J., Villar, M.V., et al. The hydration of bentonite buffer material revealed by modeling analysis of a long-term in situ test. Applied Clay Science 2020;185:105360. doi:https://doi.org/10.1016/j.clay.2019.105360.

[46] Lloret, A., Villar, M.V., Sánchez, M., Gens, A., Pintado, X., Alonso, E.. Mechanical behaviour of heavily compacted bentonite under high suction changes. Géotechnique 2003;53(1):27–40. doi: https://doi.org/10.1680/geot.2003.53.1.27.

[47] Holtz, R.D., Kovacs, W.D.. An Introduction to Geotechnical Engineering. New Jersey: Prentice Hall; 1st ed.; 1982.

[48] Zheng, L., Rutqvist, J., Birkholzer, J.T., Liu, H.H.. On the impact of temperatures up to 200 °C in clay repositories with bentonite engineer barrier systems: A study with coupled thermal, hydrological, chemical, and mechanical modeling. Engineering Geology 2015;197:278–295. doi: https://doi.org/10.1016/j.enggeo.2015.08.026.

[49] Zheng, L., Li, L., Rutqvist, J., Liu, H., Birkholzer, J.T.. Modeling radionuclide transport in clays. Tech. Rep.; FCRD-URD-2012-000128, Lawrence Berkeley National Laboratory; 2012.

[50] Liu, H., Houseworth, J., Rutqvist, J., Zheng, L., Asahina, D., Li, L., et al. THMC modeling of the near field evolution of a generic clay repository: Model validation and demonstration. Tech. Rep.; FCRD-UFD-2013-0000244, Lawrence Berkeley National Laboratory; 2013.

[51] Zheng, L., Rutqvist, J., Steefel, C., Kim, K., Chen, F., Vilarrasa, V., et al. Investigation of coupled processes and impact of high temperature limits in argillite rock. Tech. Rep.; FCRD-UFD-2014-000493, Lawrence Berkeley National Laboratory; 2014.

[52] Xu, T., Spycher, N., Sonnenthal, E., Zhang, G., Zheng, L., Pruess, K.. TOUGHREACT version 2.0: A simulator for subsurface reactive transport under non-isothermal multiphase flow conditions. Computers & Geosciences 2011;37(6):763–774. doi: https://doi.org/10.1016/j.cageo.2010.10.007.

[53] Gens, A.. Soil-environment interactions in geotechnical engineering. Géotechnique 2010;60(1):3–74. doi: https://doi.org/10.1680/geot.9.P.109.

[54] Itasca, . FLAC3D, Fast Lagrangian Analysis of Continua in 3 Dimensions. Itasca Consulting Group; Minneapolis, Minnesota; 4.0 ed.; 2009.

[55] Castellanos, E., Villar, M.V., Romero, E., Lloret, A., Gens, A.. Chemical impact on the hydro-mechanical behavior of high-density FEBEX bentonite. Physics and Chemistry of the Earth, Parts A/B/C 2008;33(1):S516 – S526. doi:https://doi.org/10.1016/j.pce.2008.10.056.

[56] Lauber, M., Baeyens, B., Bradbury, M.H.. Physico-Chemical Characterisation and Sorption Measurements of Cs, Sr, Ni, Eu, Th, Sn and Se on Opalinus Clay from Mont Terri (PSI Bericht). Paul Scherrer Institut; 2000. ISBN 1019-0643.

[57] Zheng, L., Kim, K., Xu, H., Rutqvist, J.. DR Argillite Disposal R&D at LBNL. Tech. Rep.; FCRD-UFD-2016-000437, LBNL-1006013, Lawrence Berkeley National Laboratory; 2016.

[58] Xu, H., Rutqvist, J., Plúa, C., Armand, G., Birkholzer, J.. Modeling of thermal pressurization in tight claystone using sequential thm coupling: benchmarking and validation against in-situ heating experiments in cox claystone. Tunnelling and Underground Space Technology 2020;103(103428). doi:https://doi.org/10.1016/j.tust.2020.103428.

[59] Xu, H., Rutqvist, J., Birkholzer, J.. A study of thermal pressurization and potential for hydro-fracturing associated with nuclear waste disposal in argillaceous claystone. International Journal of Rock Mechanics & Mining Sciences 2020;(In press).

[60] Alonso, E., Vaunat, J., Gens, A.. Modelling the mechanical behaviour of expansive clays. Engineering Geology 1999;54(1–2):173–183. doi: https://doi.org/10.1016/S0013-7952(99)00079-4.